Applied Surface Science 540 (2021) 148320

Contents lists available at ScienceDirect

Applied Surface Science

journal homepage: www.elsevier.com/locate/apsusc

New insight into absorption characteristics of CO_2 on the surface of calcite, dolomite, and magnesite

Lin Tao [a], Junchen Huang [a], Davoud Dastan [b], Tianyu Wang [c,d], Jing Li [a], Xitao Yin [e,*], Qi Wang [a,*]

[a] School of Materials and Metallurgy, University of Science and Technology Liaoning, Anshan 114051, Liaoning, China
[b] School of Materials Science and Engineering, Georgia Institute of Technology, Atlanta GA-30332, USA
[c] Harvard SEAS-CUPB Joint Laboratory on Petroleum Science, Harvard University, Cambridge, MA 02138, USA
[d] State Key Laboratory of Petroleum Resources and Prospecting, China University of Petroleum (Beijing), Beijing 102249, China
[e] School of Physics and Optoelectronic Engineering, Ludong University, Yantai 264000, Shandong, China

ARTICLE INFO

Keywords:
Calcite
Dolomite
Magnesite
CO_2
Adsorption kinetic
Effective adsorption distance

ABSTRACT

An electrochemical method and multiscale simulations were used to study adsorption performances of CO_2 on the surface of three minerals (calcite, dolomite, and magnesite). Experimental results show that dolomite has the optimum adsorption performance at different temperatures due to shorter adsorption time and larger adsorption capacity. The adsorption process of CO_2 can be described by the pseudo-first-order kinetic model. The adsorption rate constant of magnesite is the largest and that of calcite is the smallest, but the adsorption rate constant of dolomite is closer to that of magnesite. Unexpectedly, multiscale simulations show that the adsorption interface of CO_2 can be divided into strong and weak adsorption layers. Under saturated adsorption conditions, the adsorption capacity of CO_2 is determined by the weak adsorption layer. Results highlight the importance of the effective adsorption distance for the first time. Furthermore, it confirms that the effective adsorption distance of calcite is the longest and that of magnesite is the shortest, but the effective adsorption distance of dolomite is closer to that of calcite. These findings could contribute to design advanced CO_2 capture and sequestration techniques for achieving both improved shale gas production as well as alleviate the greenhouse effect.

1. Introduction

Global warming has been the focal point of environmental protection caused by the rising concentration of CO_2 in atmosphere [1–3]. In order to alleviate the greenhouse effect, CO_2 capture and sequestration (CCS) technique has been considered as one of the most promising ways [3–5]. Because CCS technique can not only reduce the concentration of CO_2, but also enhance recovery of shale gas by injecting CO_2 into geological formations [6–12].

For CO_2 capture, it is mainly used in traditional heavy industries as diverse as power plants, steel plants and cement plants, which generate large amounts of flue gas (a CO_2/N_2 mixture) [3,13,14]. Currently, industrial process for CO_2 capture is according to the use of liquid sorbents, which suffers from comparatively low efficiency, toxicity, solvent loss, and equipment corrosion [15,16]. To overcome the above problems, membrane has given rise to more attention because of its advantages of energy saving and no environmental emissions [17]. Still, membrane only has good separation performance for the gases that possess large discrepancies in kinetic diameter or polarity. Separation of CO_2 from flue gas is difficult, since they have a similar kinetic diameter and no electric dipole moment [18]. Moreover, this method is costly and temperature has a great impact on its adsorption performance [19,20].

In this regard, solid sorbents are advised to be environmentally friendly materials [13,20]. CaO has low cost and high capacity of CO_2 [21]. But CaO rapidly loses its potential to capture CO_2 during repeated cycles of annealing and carbonation, on account of the impassable accumulation of calcite on the filling layer surface [22,23]. To avoid these disadvantages, calcite is considered as an ideal candidate in light of its no environment pollution, cheapness, large storage, and wide distribution. Sun et al. [24] confirmed the feasibility of calcite capturing CO_2 from flue gas by molecular dynamics (MD) simulation. Further, Tao et al. [25] achieved adsorption kinetic analysis of CO_2 on calcite surface by the electrochemical method.

For CO_2 sequestration, it can be used in an unconventional

* Corresponding authors.
E-mail addresses: yxtaj@163.com (X. Yin), wangqi8822@sina.com (Q. Wang).

https://doi.org/10.1016/j.apsusc.2020.148320
Received 27 July 2020; Received in revised form 14 September 2020; Accepted 28 October 2020
Available online 4 November 2020

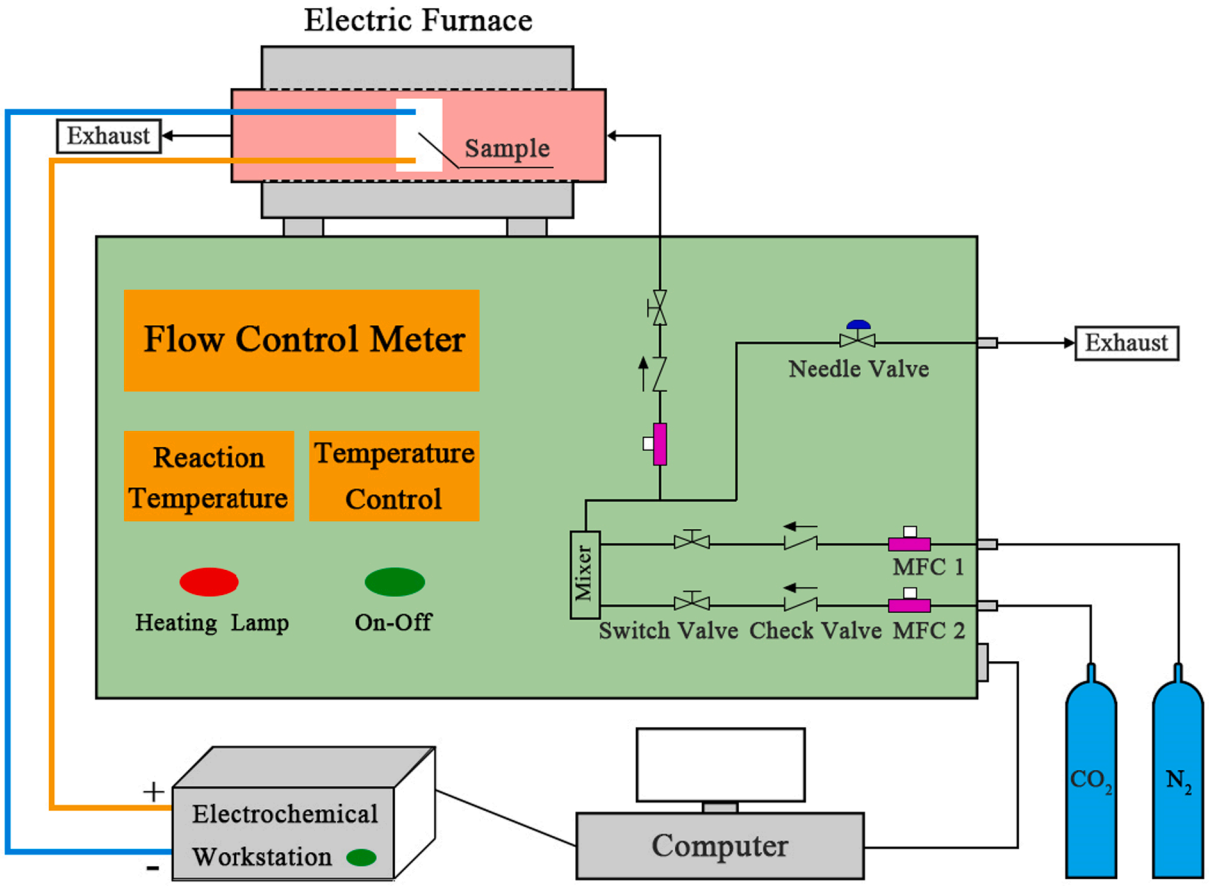

Fig. 1. Schematic diagram of experiment.

formations environment [9,26]. As shale gas is held in the pore structures of underground rocks, the injected CO_2 can displace shale gas in the pore space. Hence, CO_2 sequestration can not only enhance shale gas recovery, but also sequestrate the greenhouse gas into subsurface reservoirs. Calcite is the major constituent in the subsurface reservoirs [12,27]. Because of the complex reservoir conditions, further experiments to investigate the adsorption of CO_2 on calcite surface might be challenging [28].

Thus far, most of the researchers used simulation methods to obtain thermodynamic feasibility. For instance, Mohammed et al. [12] reported the effect of CO_2 concentration on the distribution and structure of asphaltenes in confined calcite nanopore by MD simulation. Moreover, MD simulation was used to investigate the adsorption behavior of CO_2 on the surface of calcite at various temperatures [29,30]. Stipp group [31,32] performed density functional theory (DFT) method to determine the adsorption energy on calcite surface for CO_2 molecule. Besides, Economou group [33,34] described the anisotropic behavior of CO_2 near calcite surface due to strong electrostatic interactions by MD simulation.

However, the studies of CO_2 adsorption mentioned above are all based on the ideal calcite environment and do not consider the influence of impurity Mg^{2+} because dolomite-$MgCa(CO_3)_2$ widely exists in natural environment. In other words, the isomorphism phenomenon will often occur in the crystal lattice of calcite, in which Mg^{2+} can replace Ca^{2+} at the geological conditions [35,36]. To the best of the authors' knowledge, the influence of Mg^{2+} on CO_2 adsorption behavior is rarely studied, let alone the information of adsorption kinetic. In this study, three minerals (calcite-$CaCO_3$, dolomite-$MgCa(CO_3)_2$, and magnesite-$MgCO_3$) were chosen to represent the changes in Mg^{2+} concentration, because they are the most typical natural minerals in geological environment [27,37,38].

According to the previous work [25], the electrostatic interaction between CO_2 and calcite can cause a change in electrical conductivity of calcite surface, and the law of conductivity change can be characterized by an electrochemical method. Thus, in the current work, the electrochemical technique was utilized to achieve the adsorption features of CO_2 on the surface of the aforementioned three minerals. Thereafter, the pseudo-first-order kinetic model was employed to describe the discrepancies in adsorption rates. Finally, multiscale simulations were performed to reveal mechanisms of the difference in adsorption capacities of CO_2 on the three mineral surfaces. This study will not only provide new methods for quantitative characterization of CO_2 capture and sequestration, but also propose new insights into the interaction mechanism of gas–solid interface.

2. Experimental details

2.1. Electrochemical section

2.1.1. Preparation and characterization of samples

Three samples were made from the (1 0 4) cleave surfaces of calcite, dolomite, and magnesite crystals, because the (1 0 4) cleave surface is the most thermodynamically stable crystallographic plane [35,39]. Then, three samples were checked by X-ray diffraction (XRD) (PANalytical X, RigakuD/max-Ra with CuKα, λ = 0.15418 nm). As shown in **Figure S1**, the pure calcite, dolomite, and magnesite phases were well ascertained.

2.1.2. Apparatus

A home-made experimental apparatus [40–43] including a gas mass flow controller (MFC), a tube electric furnace with a diameter of 38 mm (operation temperature range: 298 to 1273 K), temperature-control software, and an electrochemical workstation (CHI660E, Chenhua

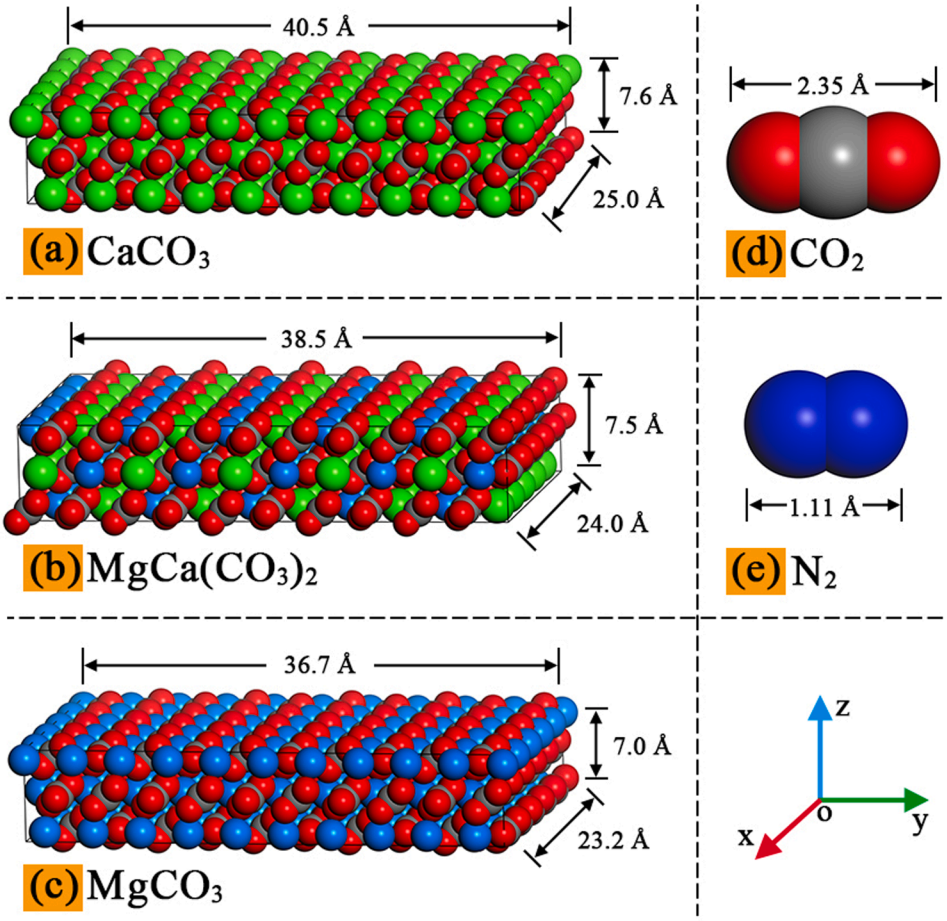

Fig. 2. Structures and parameters of three mineral surfaces as well as two gas molecules. The atomic designations are Ca (green), Mg (light blue), C (grey), N (blue), and O (red).

Instruments, Inc., China) were used to obtain all electrochemical graphs (Fig. 1).

2.1.3. Electrochemical test process

Initially, two platinum electrodes were connected on the (1 0 4) surface of specimen, and then, the sample was placed in the electrical furnace and fixed for the measurements. Next, the specimen was annealed to the desired temperature (473, 523, 573, 623, and 673 K) at a rate of 5 K/min in presence of N_2 gas (99.99%, 500 mL/min). The measurements were run for 1200 s and the CO_2 gas (99.99%, 500 mL/min) was flown into the tube using mass flow apparatus at 600 s. An electrochemical workstation was employed to measure the electrical properties of three minerals in presence of nitrogen as well as binary mixed gas at a constant voltage of 5 V. Each measurement was repeated thrice to make sure the repeatability of the obtained results.

2.2. Simulation section

2.2.1. Molecular dynamics simulation model and details

First, structures of three minerals were obtained from Materials Studio software package, and their lattice parameters were demonstrated in **Figure S2**. The initial structures and parameters of three (1 0 4) surfaces and two gas molecules were illustrated in Fig. 2. The whole adsorption structure contained a (1 0 4) mineral surface and a vacuum region of 50 Å (**Figure S3**). Mixed binary gases of N_2 and CO_2 in a 1:1 ratio was flown into a vacuum tube exposed to the mineral surface. In all MD simulations, we posited that the upper layer of the mineral surface was free and the remaining atoms were considered fixed [25,44]. A three-site model with three partial charges was defined for carbon dioxide while a two-site model with Lennard-Jones parameters was introduced to evaluate the neutral N_2 [45]. Afterwards, the COMPASS force field and Forcite module were employed in carbon dioxide adsorption systems [46,47].

This force field is the first ab initio force field which precisely predicts thermophysical and structural features for various inorganic and organic materials [48–50]. The short-range van der Waals and the long-range electrostatic interlayers were evaluated by the Lennard-Jones 9–6 function and the Columbic interactions, respectively. The Columbic and Lennard-Jones 9–6 interlayers were assessed via the Ewald and the atom-based techniques, respectively. The number, volume, and temperature parameters were considered constant for all the performed simulations. The temperature was controlled by nose thermostat. Based on the fact that the mean time is proportional to the ensemble average [28], the Boltzmann distribution and the initial velocity of the gas molecules were identical. The calculation steps of 5×10^6 was considered in each MD simulation. The time step and the total simulation time were 1 fs and 5 ns, respectively. The equilibration was achieved in the first 4 ns, and data analysis was performed in the last 1 ns. Three independent runs of 1 ns after the equilibration were used to obtain the statistical analysis for every adsorption structure.

2.2.2. First-principle calculation model and details

First, CO_2 molecules are adsorbed on the three mineral surfaces in vertical configuration based on our previous studies [25,51]. Considering the different physicochemical properties of Ca^{2+} and Mg^{2+}, two CO_2 molecules were selected to be adsorbed on the three mineral surfaces, and then their average values were calculated. Initial adsorption configurations of CO_2 on the three mineral surfaces and their lattice parameters were shown in Fig. 3. A vacuum region of 20 Å

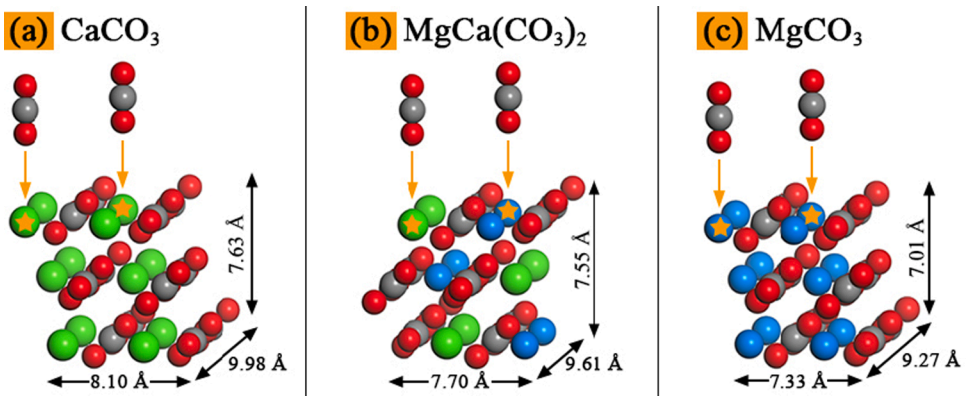

Fig. 3. Initial adsorption configurations of CO_2 and lattice parameters of three mineral surfaces. The pentagram represents the adsorption site of CO_2.

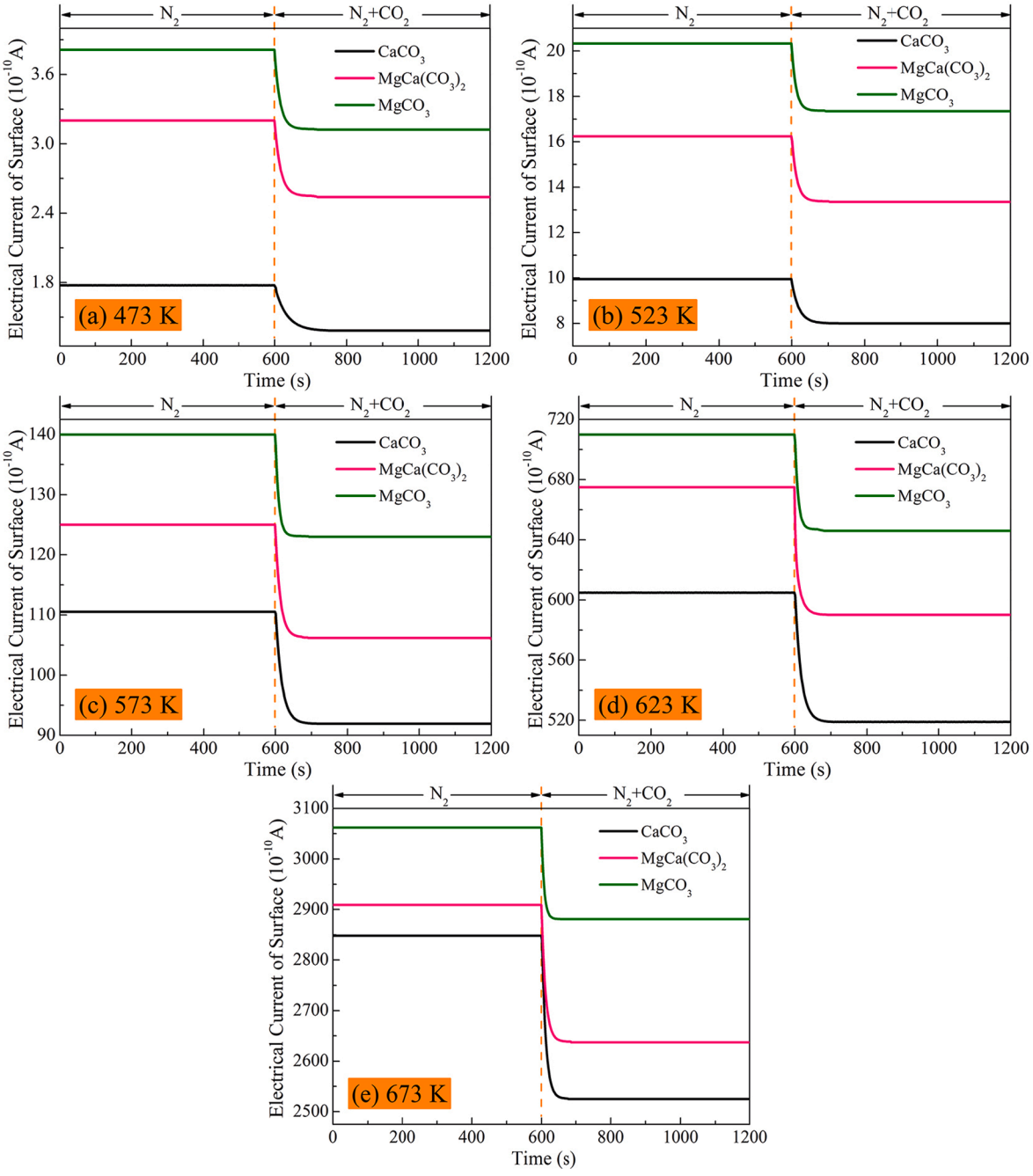

Fig. 4. Electrical currents of three mineral surfaces at different temperatures.

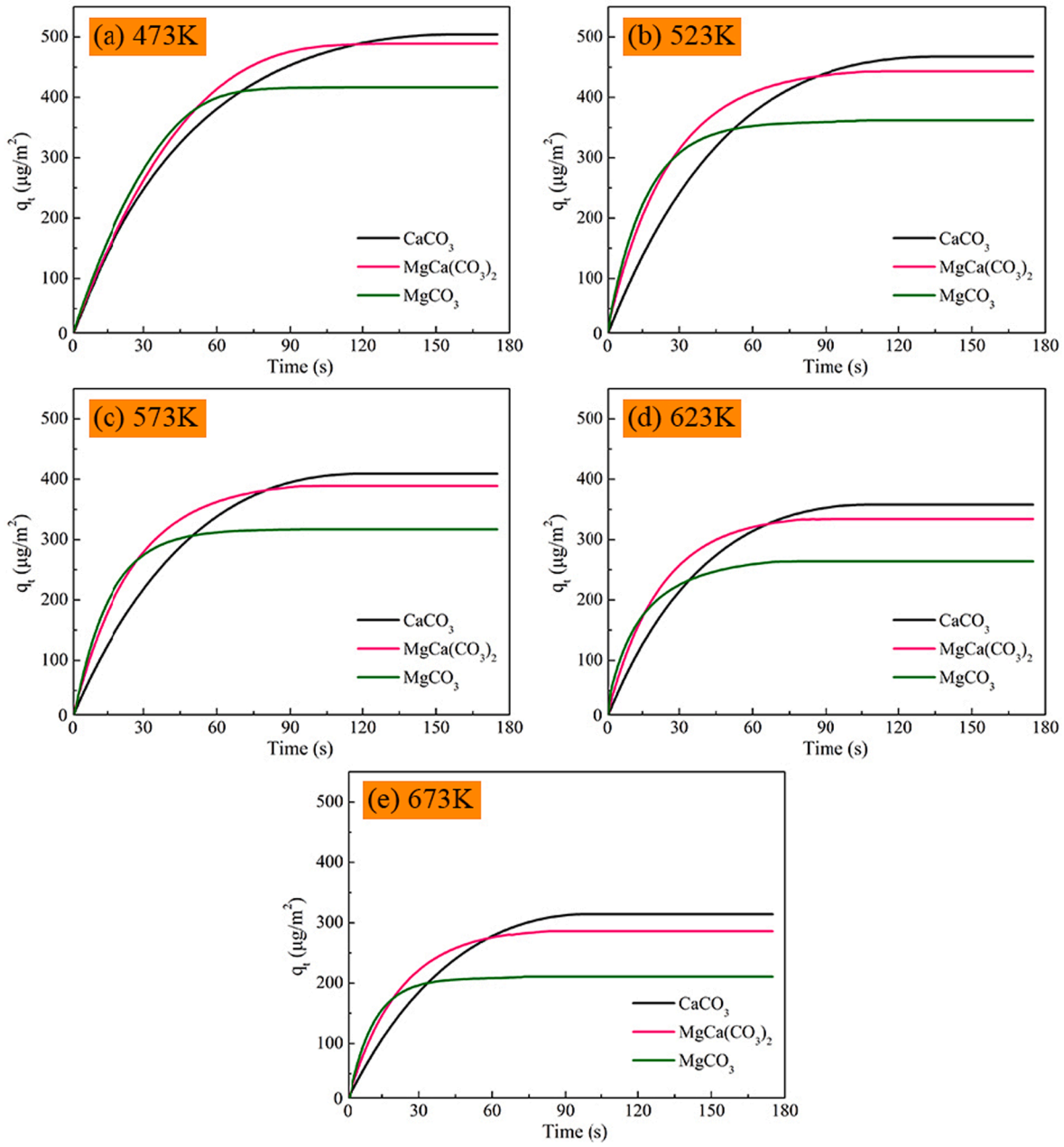

Fig. 5. Adsorption capacity of CO_2 as a function of time at different temperatures.

perpendicular to a (1 0 4) surface was used to avoid interactions between periodic structures.

Then, adsorption properties of CO_2 on mineral surfaces were calculated by Dmol^3 module, within the framework of the DFT [52,53]. The exchange–correlation interaction was calculated by the generalized gradient approximation (GGA) with the Perdew-Burke-Ernzerhof (PBE) exchange functional [54]. In order to accurately describe weak interactions, a dispersion-corrected DFT (DFT-D) method with the Grimme vdW correction was adopted in all calculations [55]. Besides, the real-space global cut-off radius was 4.9 Å and the Brillouin zone was sampled by 2 × 2 × 1 k-points using the Monkhorst-Pack scheme.

Table 1
Adsorption capacity and response time of CO_2 on three mineral surfaces at different temperatures.

Temperature (K)	Adsorption capacity (μg/m^2)			Response time (s)		
	$CaCO_3$	MgCa $(CO_3)_2$	$MgCO_3$	$CaCO_3$	MgCa $(CO_3)_2$	$MgCO_3$
473	504	485	426	160	126	119
523	467	438	367	142	110	105
573	409	389	315	125	101	92
623	358	334	264	109	92	80
673	314	282	211	100	85	70

Table 2
Rate constant k_1 obtained from the pseudo-first-order kinetic mode.

Rate constant (s^{-1})	Temperature (K)				
	473	523	573	623	673
$k_1(CaCO_3)$	0.0272	0.0314	0.0342	0.0386	0.0412
$k_1(MgCa(CO_3)_2)$	0.0294	0.0331	0.0365	0.0406	0.0431
$k_1(MgCO_3)$	0.0306	0.0348	0.0387	0.043	0.0461

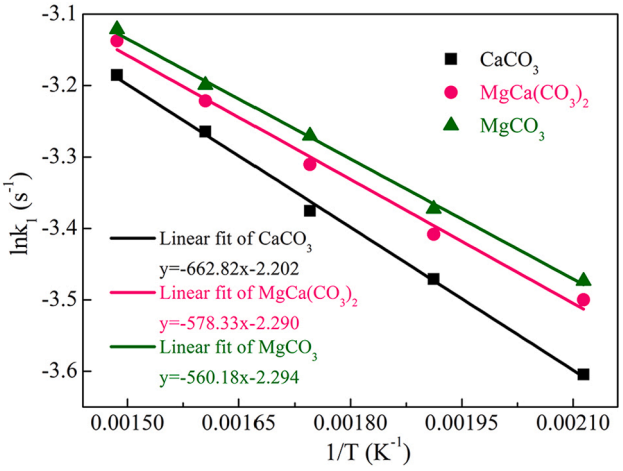

Fig. 6. Linear dependence between k_1 and $1/T$ for calculating adsorption activation energies of CO_2 on three mineral surfaces.

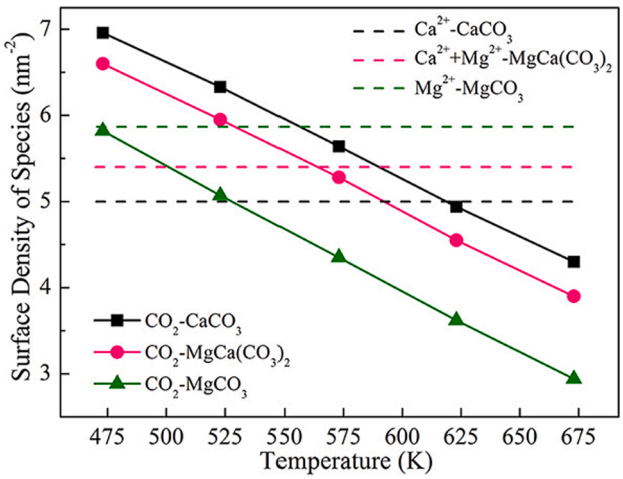

Fig. 7. Surface density of CO_2 and cations (Ca^{2+}, Mg^{2+}) as a function of temperature.

Table 3
Adsorption activation energies of CO_2 on three mineral surfaces.

	$CaCO_3$	$MgCa(CO_3)_2$	$MgCO_3$
E_a(kJ/Mol)	5.51	4.81	4.66

3. Results and discussion

3.1. Results of electrochemical experiments

Based on our previous work [25], the change in electrical current of $CaCO_3$ surface can reflect the adsorption process of CO_2 in situ. The more the electrical current changes, the more the adsorption capacity is. Moreover, the shorter the response time needs, the faster the adsorption rate is. Therefore, we first measured the changes in electrical current caused by adsorption of CO_2 on three mineral surfaces through an electrochemical method at different temperatures. Experimental results are shown in Fig. 4. Before 600 s, the electrical currents of three mineral surfaces keep in the equilibrium state under N_2 condition. At 600 s, CO_2 is gradually adsorbed on the mineral surfaces.

The adsorption of CO_2 makes significant changes in the electrical currents of three mineral surfaces. Obviously, when the electrical currents of the three mineral surfaces reach an equilibrium state, the time spent at each temperature is different. As the temperature increases, the time required to reach equilibrium is shortened. This indicates that the adsorption rates of CO_2 on the three minerals are dissimilar and the increase of temperature accelerates the adsorption rate. In addition, the variation ranges of electrical currents caused by CO_2 adsorption are also diverse, which suggests significant differences in the adsorption capacity of CO_2. The above phenomenon proves that the adsorption of CO_2 on the surface of three minerals shows different adsorption characteristics.

Furthermore, the adsorption capacity of CO_2 as a function of time can be obtained according to the relationship between the change process of the electrical current and the equilibrium adsorption capacity. Details of the calculation can be found in the authors' previous article [25]. The transformed experimental results are shown in Fig. 5 where the change in the processes of CO_2 adsorption capacity on three mineral surfaces from 0 to the maximum is evidently demonstrated. Among which, the horizontal curves indicate that the adsorption capacities of CO_2 are close to the equilibrium state. To compare the adsorption performances of CO_2 on the surface of three minerals more accurately, adsorption capacity and response time are calculated and the results are presented in Table 1.

As can be seen from Table 1, both of the CO_2 adsorption capacities and the response time decrease after increasing the temperature. Evidently, the adsorption capacities of $MgCa(CO_3)_2$ are closer to those of $CaCO_3$, and higher than those of $MgCO_3$. Besides, the response time of CO_2 on $MgCa(CO_3)_2$ are closer to those of $MgCO_3$, which are smaller than those of $CaCO_3$. Therefore, compared with the other two minerals, $MgCa(CO_3)_2$ has the optimum adsorption performance at different temperatures because of shorter adsorption time and larger adsorption capacity. To clarify the underlying mechanism, in **Section 3.2**, a kinetic model is used to explain the differences in adsorption rates. In **Section 3.3**, multiscale simulations are performed to elucidate the root causes of different adsorption capacities.

3.2. Adsorption kinetic

The pseudo-first-order kinetic model was used to obtain the kinetic parameters. It is described by the following equation:

$$\frac{dq}{dt} = k_1(q_e - q_t) \tag{1}$$

where q_e and q_t are the equilibrium adsorption capacity (μg/m^2) and the adsorption capacity at time t, respectively, t is the adsorption time (s), and k_1 is the pseudo-first-order rate constants (s^{-1}). The above equation converts to the formula (2) after applying the boundary condition (t = 0, q = 0; t = t, q = q):

$$ln(q_e - q_t) = lnq_e - k_1 t \tag{2}$$

The value of evaluated using the above equation is reliable as the pseudo-first-order kinetic model is applicable for these three minerals. As illustrated in Table 2, the adsorption rate of three minerals increased upon raised the temperature from 473 to 673 K and the constant of the adsorption rate raised for $CaCO_3$ from 0.0272 to 0.0412 s^{-1}. Meanwhile, the constant of the adsorption rate raised for $MgCa(CO_3)_2$ and $MgCO_3$ from 0.0294 to 0.0431 s^{-1} and from 0.0306 to 0.0461 s^{-1}, respectively. Based on the above results, the adsorption rate of $MgCO_3$ is the fastest while that of $CaCO_3$ is the slowest. Importantly, the adsorption rate constants of $MgCa(CO_3)_2$ are closer to those of $MgCO_3$, reaching over 90%. This clearly explains that the response time of $MgCa(CO_3)_2$ is as short as that of $MgCO_3$. Furthermore, the influence of temperature on the adsorption rate can be characterized by adsorption activation energy. The adsorption activation energies of CO_2 on three mineral

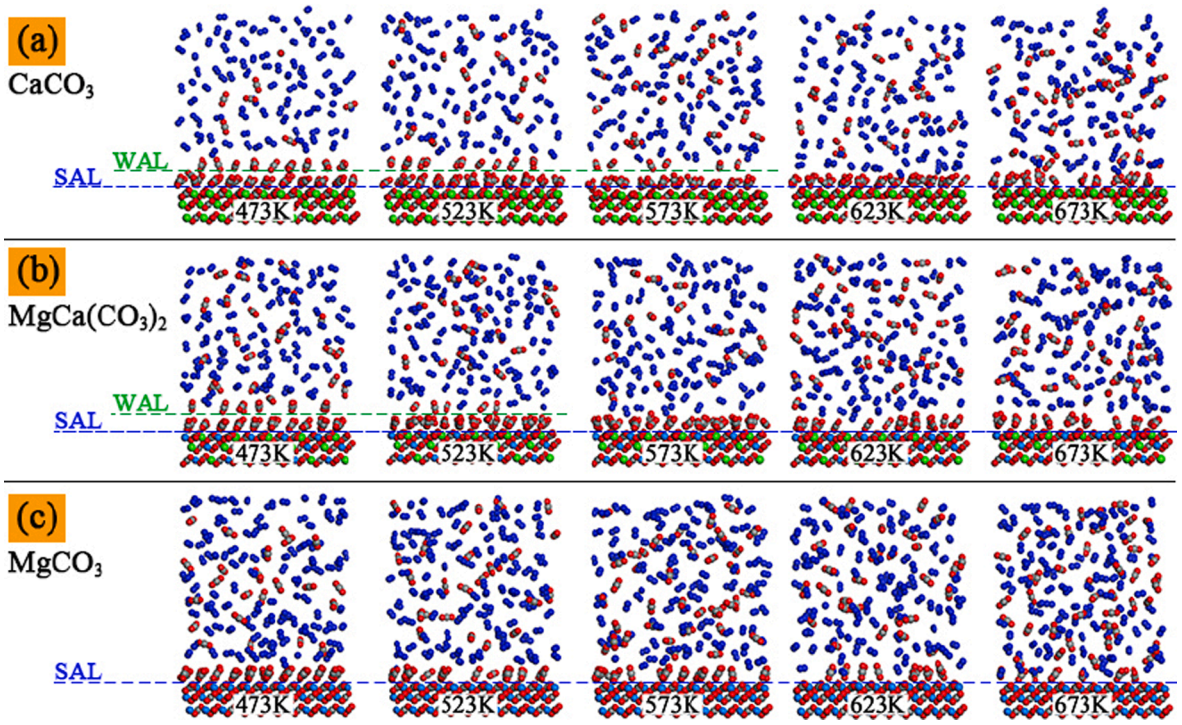

Fig. 8. Snapshots of interface adsorption structures of (a) CO_2-$CaCO_3$, (b) CO_2-$MgCa(CO_3)_2$, and (c) CO_2-$MgCO_3$ systems at different temperatures. SAL, strong adsorption layer; and WAL, weak adsorption layer.

surfaces were calculated based on the Arrhenius equation as follow:

$$k_1 = Aexp(-E_a/RT) \quad (3)$$

where A, E_a, and R refer to the Arrhenius factor (s^{-1}), Arrhenius activation energy (kJ/mol), and gas constant (8.314 J/mol/K), respectively. Next, Eq. (3) can be expressed as;

$$lnk_1 = lnA - E_a/RT \quad (4)$$

Bring the data from Table 2 into Eq. (4), the linear dependence between In k_1 and $1/T$ can be obtained in Fig. 6. Finally, the adsorption activation energies of CO_2 on three mineral surfaces which were obtained from the slope of the plot in Fig. 6 are demonstrated in Table 3. The adsorption activation energy of CO_2 on $CaCO_3$ is the largest, so the temperature has the greatest influence on the adsorption rate of CO_2 on $CaCO_3$ surface. However, because the adsorption activation energies of CO_2 on $MgCa(CO_3)_2$ and $MgCO_3$ are similar and smaller than those of $CaCO_3$, the effect of the temperature on the adsorption rates of CO_2 on $MgCa(CO_3)_2$ and $MgCO_3$ are less than those of $CaCO_3$. Thus, the thermal stability of CO_2 adsorbed on $MgCa(CO_3)_2$ is similar to that on $MgCO_3$.

3.3. Gas-solid interface interaction

In this section, to investigate the mechanism of differences in adsorption capacities of CO_2 on the three minerals, the detailed structures of the gas–solid interface are first obtained by MD simulation. Thereupon, the potential energy curves of CO_2 on the three mineral surfaces are calculated by DFT. Finally, the potential mechanism of differences in adsorption capacity is proposed.

3.3.1. Structure of adsorption layer

The surface densities of carbon dioxide and cations are evaluated in order to demonstrate the structure of gas–solid interface. Because the surface density can describe both the adsorption structure as well as the equilibrium adsorption capacity. The surface density is described as the amount of species (metal cations or CO_2 molecule) on mineral surface upon the mineral surface area. Fig. 7 shows the surface densities of CO_2 and cations on the surface of three minerals at various temperatures. First, the surface densities of CO_2 on $MgCa(CO_3)_2$ are closer to those of $CaCO_3$ and larger than those of $MgCO_3$. Secondly, in addition to $MgCO_3$, the surface densities of CO_2 are greater than those of cations (Ca^{2+}/Mg^{2+}) on $CaCO_3$ and $MgCa(CO_3)_2$ at low temperatures. It indicates that CO_2 gas can form the double-layer adsorption structures on the surface of $CaCO_3$ and $MgCa(CO_3)_2$ at low temperatures. However, as the temperature rises, CO_2 begins to dissociate from the surface. When the temperature exceeds 523 K, CO_2 gas becomes a single-layer adsorption structure on $MgCa(CO_3)_2$. When the temperature rises to 573 K, CO_2 gas shows a single-layer adsorption structure on $CaCO_3$.

To clarify the interface structures, the snapshots of CO_2 adsorption equilibrium on the three mineral surfaces were obtained in detail at different temperatures. Fig. 8 displays that the double-layer adsorption structures of CO_2 are found on the surface of $CaCO_3$ and $MgCa(CO_3)_2$, and a single-layer adsorption structure of CO_2 is formed on $MgCO_3$ surface. Besides, the highly oriented arrangement of CO_2 molecules close to the surface of three minerals, it can be attributed to the strong electrostatic interactions between CO_2 and the mineral surface [2,33,34]. As the temperature rises, CO_2 gradually begins to dissociate from the surface of the three minerals. N_2 molecules are hardly adsorbed on the surface of three minerals, then it presents the whole phase. Therefore, the adsorption interface of CO_2 is divided into a strong adsorption layer (SAL) and a weak adsorption layer (WAL).

Furthermore, in the SAL, not only a single CO_2 molecule is adsorbed on a single Ca^{2+}, but also a single CO_2 molecule is adsorbed on a single Mg^{2+}. This phenomenon indicates that the surface density of CO_2 is equal to the surface density of cation under a single-layer saturated adsorption. Therefore, it can be concluded that the difference in adsorption capacities of CO_2 on the three minerals is determined by the adsorption capacity of WAL. Moreover, we believe that the distance of electrostatic interaction exceeds the thickness of the SAL. We speculate that the difference in adsorption capacity of CO_2 is related to the structure of mineral surface and the effective adsorption distance. Here, the effective adsorption distance refers to the distance where the

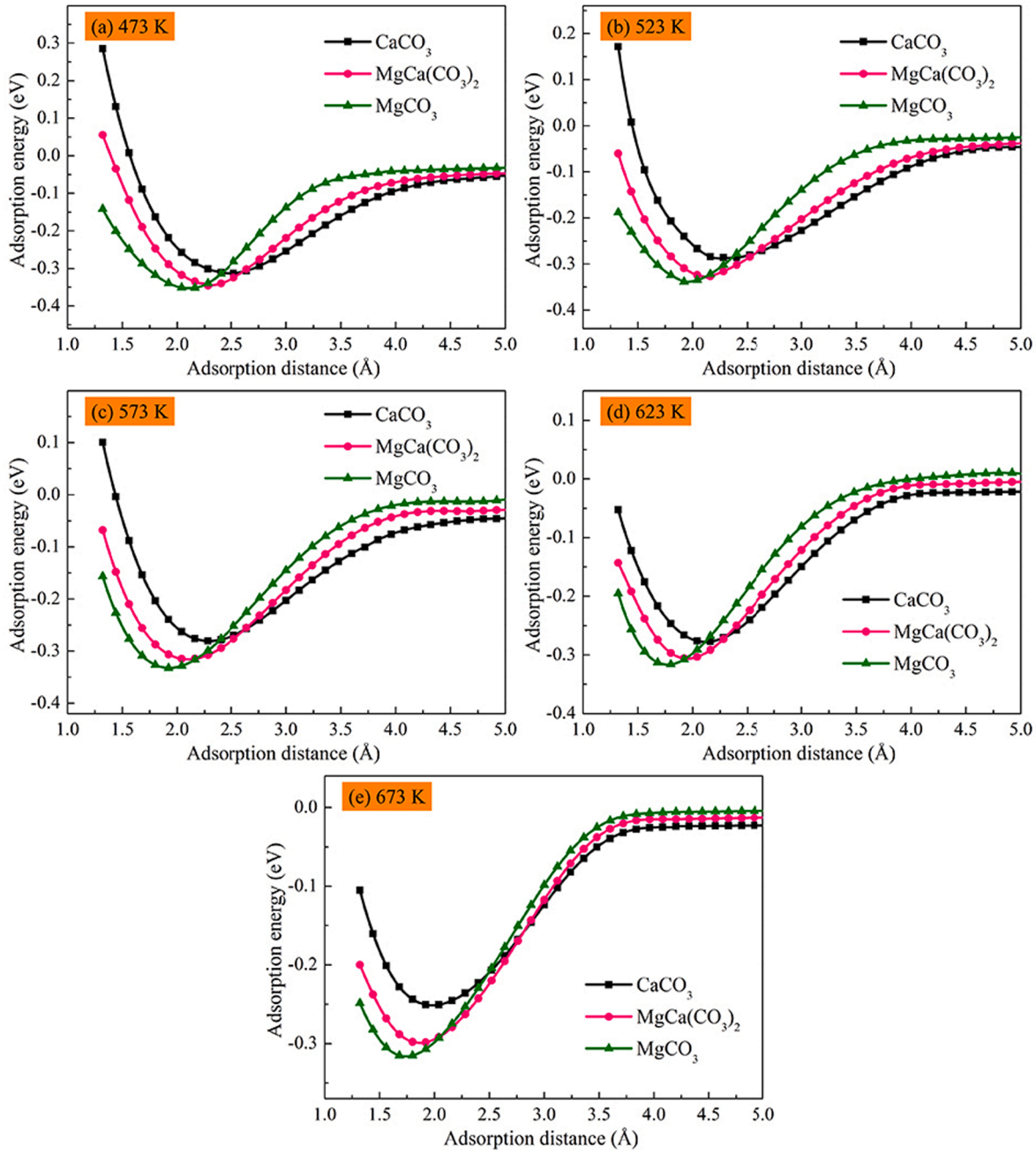

Fig. 9. Potential energy curves for CO_2 approaching the three mineral surfaces at different temperatures.

adsorption energy is greater than the adsorption activation energy (energy barrier), when CO_2 is close to the mineral surface. If the result is the opposite, CO_2 cannot be adsorbed on the surface. It should be noted that the adsorption activation energy can represent the energy barrier to be overcome during the gas adsorption [25,56,57]. To verify our hypothesis, the structures of three mineral surfaces and the potential energy curves should be obtained at different temperatures.

3.3.2. *Potential energy curves*

In this section, the reconstructed structures of three mineral surfaces are first obtained at different temperatures. Then, the potential energy curves of CO_2 on three mineral surfaces are calculated. Finally, the underlying mechanism of the differences in adsorption capacities of CO_2 on three mineral surfaces is proposed.

First of all, MD simulation was performed to realize the reconstructed structures of the three mineral surfaces at different temperatures, while DFT method is limited by temperature, accessible time, and system size [25,58]. **Figure S4** shows the rotating and distorting carbonates on topmost layer of the three mineral surfaces, and the metal cations also deviate from their ideal positions. It can be attributed to the increased surface energy resulting from the termination of periodic structures within the bulk phase. To minimize the surface energy, the atoms rearrange and often the symmetry of the resulting structure is different from that of the bulk phase [59,60].

DFT calculation is often used to calculate adsorption energy and to reveal the behavior of gas–solid interface. The adsorption energy is defined as

$$E_{ads} = E_{total} - \left(E_{surface} + E_{gas}\right) \quad (5)$$

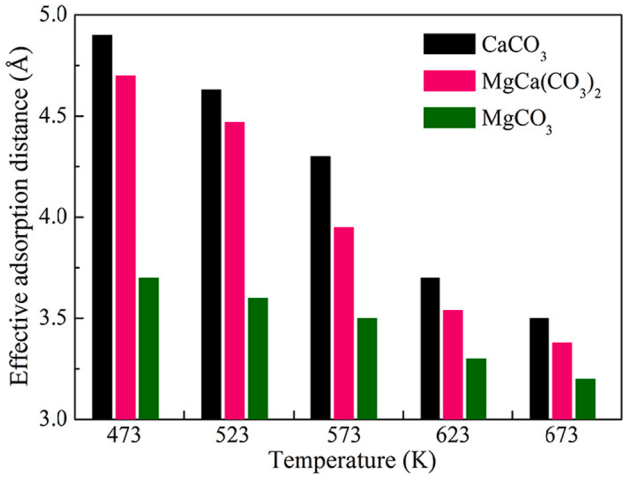

Fig. 10. Effective adsorption distances of CO_2 on three mineral surfaces at different temperatures.

where E_{ads} is the adsorption energy (eV), E_{total} is the single point energy of gas-surface system (eV), $E_{surface}$ is the single point energy of mineral surface (eV), and E_{gas} is the single point energy of gas molecular system (eV). A more negative value represents a more powerful interaction between gas molecule and the mineral surface. By comparing the adsorption energies at different sites [51], we found the effect of the position on the adsorption energy is almost negligible. Here, the configurations of CO_2 adsorbed on the three mineral surfaces are designed in Fig. 3. Based on the reconstructed structures of three mineral surfaces in **Figure S4**, adsorption energies of CO_2 on three mineral surfaces as a function of adsorption distance are depicted in Fig. 9 and **Tables S1-S5**.

For the three minerals in Fig. 9, CO_2 reaches into the attractive well (adsorption equilibrium position) as the adsorption distance decreases. As the distance decreases further, the repulsive force increases rapidly. At the adsorption equilibrium positions of the three minerals, the order of the adsorption energy is shown as $MgCO_3 > MgCa(CO_3)_2 > CaCO_3$. From the point of view of charge distribution, the charge density map of CO_2 adsorbed on the surface of three minerals were plotted. As shown in **Figure S5-S9**, results show that CO_2 is physically adsorbed on the surface of three minerals because there is no overlap of electron clouds. In addition, the degree of charge change between CO_2 and $MgCO_3$ is the largest, which also verifies the maximum adsorption energy between CO_2 and $MgCO_3$. Interestingly, compared with experimental results of adsorption capacity (Fig. 5), $MgCO_3$ has the smallest adsorption capacity of CO_2 but the largest adsorption energy, while the results of $CaCO_3$ are just the opposite. These observations indicate that the differences in adsorption capacities of three minerals cannot be expressed simply by the adsorption energy at the adsorption equilibrium position. It is necessary to consider the attenuation distance of adsorption energy, that is, the effective adsorption distance.

The shorter the attenuation distance becomes, the smaller the adsorption capacity will be. By comparing the adsorption energy profiles at different distances, the absorption energies of $MgCO_3$ decrease faster than those of $CaCO_3$ when CO_2 is far from the surface, so the effective adsorption distances of $MgCO_3$ are less than those of $CaCO_3$. Interestingly, the effective adsorption distances of $MgCa(CO_3)_2$ are closer to those of $CaCO_3$. To illustrate the underlying mechanisms of the differences in adsorption capacity more clearly, we accurately measured the distances where the adsorption energy is greater than the adsorption activation energy. For the adsorption activation energies of CO_2 on three minerals, they come from the values in Table 3. When the unit of adsorption activation energy is converted into eV, the adsorption activation energies of CO_2 on $CaCO_3$, $MgCa(CO_3)_2$, and $MgCO_3$ are 0.057, 0.050, and 0.048 eV, respectively.

By comparing adsorption activation energies with adsorption energies in Fig. 9, the effective adsorption distances of CO_2 on three mineral surfaces are shown in Fig. 10. As the temperature rises, all of the effective adsorption distances decrease so that CO_2 molecules gradually begin to dissociate from the surface of the three minerals. After the temperature exceeds 573 K, CO_2 gas presents the single-layer adsorption structure on $CaCO_3$. For $MgCa(CO_3)_2$, CO_2 gas keeps a double-layer adsorption structure until temperature exceeds 523 K to become a single-layer. Significantly, CO_2 can only be adsorbed in WAL when the adsorption energy of WAL is greater than its adsorption activation energy. Since the adsorption energies of WAL on $MgCO_3$ do not exceed the adsorption activation energy, CO_2 gas presents the single-layer adsorption structure on $MgCO_3$ in the whole temperature range. In addition, at each temperature, the effective adsorption distance of $CaCO_3$ is the longest and that of $MgCO_3$ is the shortest. Importantly, the effective adsorption distance of $MgCa(CO_3)_2$ accounts for more than 90% of that of $CaCO_3$. Therefore, the adsorption capacity of $MgCa(CO_3)_2$ is closer to that of $CaCO_3$.

4. Conclusions

The electrochemical method and multiscale simulations were performed to study the adsorption performances of CO_2 on the surface of $CaCO_3$, $MgCa(CO_3)_2$, and $MgCO_3$. Experimental results show that $CaCO_3$ has the maximum adsorption capacity, but its adsorption rate is the smallest. Instead, $MgCO_3$ has the largest adsorption rate, but its adsorption capacity is the smallest. Interestingly, $MgCa(CO_3)_2$ has the optimum adsorption performances owing to the advantages of faster adsorption rate and larger adsorption capacity. To clarify the underlying mechanism of the differences in the adsorption performances, the pseudo-first-order kinetic model was used to explain the differences in adsorption rates. Results show that the adsorption rate constant of $MgCO_3$ is the largest. The adsorption rate constants of $MgCa(CO_3)_2$ are closer to those of $MgCO_3$, reaching over 90%. Next, multiscale simulations were performed to reveal mechanisms of the difference in adsorption capacities. Simulation results show that the adsorption interface of CO_2 is divided into a strong adsorption layer (SAL) and a weak adsorption layer (WAL). By comparing the potential energy curves, for the first time, we highlight the importance of effective adsorption distance in clarifying the difference in adsorption capacity. The effective adsorption distance of $CaCO_3$ is the longest. The effective adsorption distances of $MgCa(CO_3)_2$ are closer to those of $CaCO_3$, reaching over 90%. Therefore, the above results demonstrate that $MgCa(CO_3)_2$ has the optimum adsorption performances because of larger adsorption rate constants and longer effective adsorption distances.

CRediT authorship contribution statement

Lin Tao: Conceptualization, Methodology, Formal analysis, Writing - original draft. **Junchen Huang:** Formal analysis, Writing - review & editing. **Davoud Dastan:** Formal analysis, Writing - review & editing. **Tianyu Wang:** Writing - review & editing. **Jing Li:** Resources, Visualization. **Xitao Yin:** Conceptualization, Supervision, Resources. **Qi Wang:** Methodology, Writing - review & editing, Software, Resources.

Declaration of Competing Interest

The authors declare that they have no known competing financial interests or personal relationships that could have appeared to influence the work reported in this paper.

Acknowledgements

The funding from the National Natural Science Foundation of China (Grant No. 51634004, 51874169 and 51974157) is gratefully acknowledged.

Appendix A. Supplementary material

Supplementary data to this article can be found online at https://doi.org/10.1016/j.apsusc.2020.148320.

References

[1] J. Jia, Y. Liang, T. Tsuji, C.R. Miranda, Y. Masuda, T. Matsuoka, Ab Initio Molecular Dynamics Study of Carbonation and Hydrolysis Reactions on Cleaved Quartz (001) Surface, J. Phys. Chem. C 123 (2019) 4938–4948.

[2] S. Kwon, H.J. Kwon, J.I. Choi, K.C. Kim, J.G. Seo, J.E. Park, S.J. You, E.D. Park, S. S. Jang, H.C. Lee, Enhanced selectivity for CO_2 adsorption on mesoporous silica with alkali metal halide due to electrostatic field: A molecular simulation approach, ACS Appl. Mater. Interf. 9 (2017) 31683–31690.

[3] Y.S. Bae, R.Q. Snurr, Development and evaluation of porous materials for carbon dioxide separation and capture, Angew. Chem. 50 (2011) 11586–11596.

[4] D.W. Keith, Why Capture CO_2 from the Atmosphere? Science 325 (2009) 1654–1655.

[5] J.M. Jang, S.G. Kang, Understanding CO_2 Adsorption on a M1 (M2)-Promoted (Doped) MgO–CaO(100) Surface (M1 = Li, Na, K, and Rb, M2 = Sr): A DFT Theoretical Study, ACS Sustain. Chem. Eng. 7 (2019) 16979–16984.

[6] T. Wang, S. Tian, G. Li, M. Sheng, W. Ren, Q. Liu, S. Zhang, Molecular Simulation of CO_2/CH_4 Competitive Adsorption on Shale Kerogen for CO_2 Sequestration and Enhanced Gas Recovery, J. Phys. Chem. C 122 (2018) 17009–17018.

[7] T. Fang, M. Wang, J. Li, B. Liu, Y. Shen, Y. Yan, J. Zhang, Study on the Asphaltene Precipitation in CO_2 Flooding: A Perspective from Molecular Dynamics Simulation, Ind. Eng. Chem. Res. 57 (2018) 1071–1077.

[8] W. Zhou, H. Wang, Y. Yan, X. Liu, Adsorption Mechanism of CO_2/CH_4 in Kaolinite Clay: Insight from Molecular Simulation, Energy Fuels 33 (2019) 6542–6551.

[9] M. Zhang, S. Zhan, Z. Jin, Recovery mechanisms of hydrocarbon mixtures in organic and inorganic nanopores during pressure drawdown and CO_2 injection from molecular perspectives, Chem. Eng. J. 382 (2020), 122808.

[10] J.J. Sheng, Enhanced oil recovery in shale reservoirs by gas injection, J. Nat. Gas Sci. Eng. 22 (2015) 252–259.

[11] S.B. Badmos, T. Bui, A. Striolo, D.R. Cole, Factors Governing the Enhancement of Hydrocarbon Recovery via H_2S and/or CO_2 Injection: Insights from a Molecular Dynamics Study in Dry Nanopores, J. Phys. Chem. C 123 (2019) 23907–23918.

[12] S. Mohammed, G. Gadikota, The influence of CO_2 on the structure of confined asphaltenes in calcite nanopores, Fuel 236 (2019) 769–777.

[13] A. Samanta, A. Zhao, G.K. Shimizu, P. Sarkar, R. Gupta, Post-combustion CO_2 capture using solid sorbents: a review, Ind. Eng. Chem. Res. 51 (2011) 1438–1463.

[14] W. Wang, Q. Hou, K. Gong, Y. Yan, J. Zhang, Ionic liquid gated 2D-CAP membrane for highly efficient CO_2/N_2 and CO_2/CH_4 separation, Appl. Surf. Sci. 494 (2019) 477–483.

[15] S. Zulfiqar, F. Karadas, J. Park, E. Deniz, G.D. Stucky, Y. Jung, M. Atilhan, C. T. Yavuz, Amidoximes: promising candidates for CO_2 capture, Energy Environ. Sci. 4 (2011) 4528.

[16] H. Yang, Z. Xu, M. Fan, R. Gupta, R.B. Slimane, A.E. Bland, I. Wright, Progress in carbon dioxide separation and capture: A review, J. Environ. Sci. 20 (2008) 14–27.

[17] J. Azamat, A. Khataee, F. Sadikoglu, Separation of carbon dioxide and nitrogen gases through modified boron nitride nanosheets as a membrane: insights from molecular dynamics simulations, RSC Adv. 6 (2016) 94911–94920.

[18] M. Shan, Q. Xue, N. Jing, C. Ling, T. Zhang, Z. Yan, J. Zheng, Influence of chemical functionalization on the CO_2/N_2 separation performance of porous graphene membranes, Nanoscale 4 (2012) 5477–5482.

[19] P. Marchetti, M.F. Jimenez Solomon, G. Szekely, A.G. Livingston, Molecular separation with organic solvent nanofiltration: a critical review, Chem. Rev. 114 (2014) 10735–10806.

[20] J. Wang, L. Huang, R. Yang, Z. Zhang, J. Wu, Y. Gao, Q. Wang, D. O'Hare, Z. Zhong, Recent advances in solid sorbents for CO_2 capture and new development trends, Energy Environ. Sci. 7 (2014) 3478–3518.

[21] B. Dou, C. Wang, Y. Song, H. Chen, B. Jiang, M. Yang, Y. Xu, Solid sorbents for in-situ CO_2 removal during sorption-enhanced steam reforming process: A review, Renew. Sustain. Energy Rev. 53 (2016) 536–546.

[22] R. Filitz, A.M. Kierzkowska, M. Broda, C.R. Müller, Highly efficient CO_2 sorbents: development of synthetic, calcium-rich dolomites, Environ. Sci. Technol. 46 (2011) 559–565.

[23] S. Wang, S. Yan, X. Ma, J. Gong, Recent advances in capture of carbon dioxide using alkali-metal-based oxides, Energy Environ. Sci. 4 (2011) 3805–3819.

[24] H. Sun, H. Zhao, N. Qi, X. Zhang, Y. Li, Exploration of Capturing CO_2 from Flue Gas by Calcite Slit-Nanopores: A Computational Investigation, Energy Technol. (2018).

[25] L. Tao, J. Huang, X. Yin, Q. Wang, Z. Li, G. Wang, B. Cui, Adsorption Kinetics of CO_2 on a Reconstructed Calcite Surface: An Experiment-Simulation Collaborative Method, Energy Fuels 33 (2019) 8946–8953.

[26] Z. Ma, P.G. Ranjith, Review of application of molecular dynamics simulations in geological sequestration of carbon dioxide, Fuel 255 (2019), 115644.

[27] T. Wang, S. Tian, G. Li, M. Sheng, W. Ren, Q. Liu, Y. Tan, P. Zhang, Experimental study of water vapor adsorption behaviors on shale, Fuel 248 (2019) 168–177.

[28] Y. Ma, G. Lu, C. Shao, X. Li, Molecular dynamics simulation of hydrocarbon molecule adsorption on kaolinite (0 0 1) surface, Fuel 237 (2019) 989–1002.

[29] P. Van Cuong, B. Kvamme, T. Kuznetsova, B. Jensen, Molecular dynamics study of calcite, hydrate and the temperature effect on CO_2 transport and adsorption stability in geological formations, Mol. Phys. 110 (2012) 1097–1106.

[30] L. Tao, Z. Li, G.-C. Wang, B.-Y. Cui, X.-T. Yin, Q. Wang, Evolution of calcite surface reconstruction and interface adsorption of calcite-CO_2 with temperature, Mater. Res. Express 6 (2018), 025035.

[31] E. Ataman, M.P. Andersson, M. Ceccato, N. Bovet, S.L.S. Stipp, Functional group adsorption on calcite: I. Oxygen containing and nonpolar organic molecules, J. Phys. Chem. C 120 (2016) 16586–16596.

[32] A. Silvestri, A. Budi, E. Ataman, M.H.M. Olsson, M.P. Andersson, S.L.S. Stipp, J. D. Gale, P. Raiteri, A Quantum Mechanically Derived Force Field To Predict CO2 Adsorption on Calcite 10.4 in an Aqueous Environment, J. Phys. Chem. C 121 (2017) 24025–24035.

[33] L.F. Franco, M. Castier, I.G. Economou, Anisotropic parallel self-diffusion coefficients near the calcite surface: A molecular dynamics study, J. Chem. Phys. 145 (2016), 084702.

[34] M.S. Santos, L.F.M. Franco, M. Castier, I.G. Economou, Molecular Dynamics Simulation of n-Alkanes and CO_2 Confined by Calcite Nanopores, Energy Fuels 32 (2018) 1934–1941.

[35] N.H. De Leeuw, Surface structures, stabilities, and growth of magnesian calcites: A computational investigation from the perspective of dolomite formation, Am. Mineral. 87 (2002) 679–689.

[36] N.H. de Leeuw, S.C. Parker, Surface–water interactions in the dolomite problem, PCCP 3 (2001) 3217–3221.

[37] E. Escamilla-Roa, C.I. Sainz-Díaz, F.J. Huertas, A. Hernández-Laguna, Adsorption of molecules onto (1014) dolomite surface: An application of computational studies for microcalorimetry, J. Phys. Chem. C 117 (2013) 17583–17590.

[38] X. Li, Q. Xue, L. Zhu, Y. Jin, T. Wu, Q. Guo, H. Zheng, S. Lu, How to select an optimal surfactant molecule to speed up the oil-detachment from solid surface: A computational simulation, Chem. Eng. Sci. 147 (2016) 47–53.

[39] C. Rodriguez-Navarro, K. Kudlacz, E. Ruiz-Agudo, The mechanism of thermal decomposition of dolomite: New insights from 2D-XRD and TEM analyses, Am. Min. 97 (2012) 38–51.

[40] X.-T. Yin, J. Li, D. Dastan, W.-D. Zhou, H. Garmestani, F.M. Alamgir, Ultra-high selectivity of H_2 over CO with a p-n nanojunction based gas sensors and its mechanism, Sens. Actuat. B 319 (2020), 128330.

[41] X.-T. Yin, W.-D. Zhou, J. Li, Q. Wang, F.-Y. Wu, D. Dastan, D. Wang, H. Garmestani, X.-M. Wang, Ş. Ţălu, A highly sensitivity and selectivity Pt-SnO_2 nanoparticles for sensing applications at extremely low level hydrogen gas detection, J. Alloy. Compd. 805 (2019) 229–236.

[42] X.-T. Yin, P. Lv, J. Li, A. Jafari, F.-Y. Wu, Q. Wang, D. Dastan, Z. Shi, S. Yu, H. Garmestani, Nanostructured tungsten trioxide prepared at various growth temperatures for sensing applications, J. Alloy. Compd. 825 (2020), 154105.

[43] X.T. Yin, D. Dastan, F.Y. Wu, J. Li, Facile Synthesis of SnO_2/$LaFeO_3$-XNX Composite: Photocatalytic Activity and Gas Sensing Performance, Nanomaterials 9 (2019).

[44] A.L. Rohl, K. Wright, J.D. Gale, Evidence from surface phonons for the (2× 1) reconstruction of the (1014) surface of calcite from computer simulation, Am. Mineral. 88 (2003) 921–925.

[45] J.J. Potoff, J.I. Siepmann, Vapor–liquid equilibria of mixtures containing alkanes, carbon dioxide, and nitrogen, AIChE J. 47 (2001) 1676–1682.

[46] H. Sun, COMPASS: an ab initio force-field optimized for condensed-phase applications overview with details on alkane and benzene compounds, J. Phys. Chem. B 102 (1998) 7338–7364.

[47] H. Sun, P. Ren, J. Fried, The COMPASS force field: parameterization and validation for phosphazenes, Comput. Theor. Polym. Sci. 8 (1998) 229–246.

[48] H. Sun, H. Zhao, N. Qi, Y. Li, Molecular Insights into the Enhanced Shale Gas Recovery by Carbon Dioxide in Kerogen Slit Nanopores, J. Phys. Chem. C 121 (2017) 10233–10241.

[49] S. Wang, G. Zhou, Y. Ma, L. Gao, R. Song, G. Jiang, G. Lu, Molecular dynamics investigation on the adsorption behaviors of H_2O, CO_2, CH_4 and N_2 gases on calcite (1 1^{-} 0) surface, Appl. Surf. Sci. 385 (2016) 616–621.

[50] T. Fang, M. Wang, C. Wang, B. Liu, Y. Shen, C. Dai, J. Zhang, Oil detachment mechanism in CO_2 flooding from silica surface: Molecular dynamics simulation, Chem. Eng. Sci. 164 (2017) 17–22.

[51] L. Tao, J. Huang, D. Dastan, T. Wang, J. Li, X. Yin, Q. Wang, CO_2 capture and separation on charge-modulated calcite, Appl. Surf. Sci. 530 (2020), 147265.

[52] B. Delley, An all-electron numerical method for solving the local density functional for polyatomic molecules, J. Chem. Phys. 92 (1990) 508–517.

[53] B. Delley, From molecules to solids with the $DMol^3$ approach, J. Chem. Phys. 113 (2000) 7756–7764.

[54] J.P. Perdew, K. Burke, M. Ernzerhof, Generalized Gradient Approximation Made Simple, Phys. Rev. Lett. 77 (1996) 3865–3868.

[55] S. Grimme, Semiempirical GGA-type density functional constructed with a long-range dispersion correction, J. Comput. Chem. 27 (2006) 1787–1799.

[56] Z. Zhao, Z. Li, Y.S. Lin, Adsorption and Diffusion of Carbon Dioxide on Metal−Organic Framework MOF-5, Ind. Eng. Chem. Res. 48 (2009) 10015–10020.

[57] Z. Zhang, S. Huang, S. Xian, H. Xi, Z. Li, Adsorption equilibrium and kinetics of CO2 on chromium terephthalate MIL-101, Energy Fuels 25 (2011) 835–842.

[58] G.R. Hantal, L. Brochard, M.N.l. Dias Soeiro Cordeiro, F.J. Ulm, R.J.-M. Pellenq, Surface chemistry and atomic-scale reconstruction of kerogen–silica composites, J. Phys. Chem. C 118 (2014) 2429–2438.

[59] G. Pacchioni, Surface reconstructions: Polaron bricklayers at work, Nat. Rev. Mater. 2 (2017) 17071.

[60] U. Diebold, Oxide surfaces: Surface science goes inorganic, Nat. Mater. 9 (2010) 185.